Peer-reviewed version available at Coatings 2019, 9, 71; doi:10.3390/coatings9020071

Article

Cracking, Microstructure and Tribological Properties of Laser Formed and Remelted K417G Ni-based Superalloy

Shuai Liu [1], Haixin Yu [1], Yang Wang [1], Xue Zhang [1], Jinguo Li [2], Suiyuan Chen [1] and Changsheng Liu [1,*]

1 School of Materials Science and Engineering, Northeastern University, Key Laboratory for Anisotropy and Texture of Materials Ministry of Education, Shenyang, China, 110819; 200804892@qq.com
2 Institute of Metal Research, Chinese Academy of Sciences, Shenyang, China, 110006; jgli@imr.ac.cn
* Correspondence: csliu@mail.neu.edu.cn; Tel.: +86-15998375588

Abstract: K417G Ni-based superalloy is widely used in aeroengine turbine blade for its excellent properties. However, the aeroengine rotor blade zigzag crown appears early failure frequently, which is because of the wear problems occurring in the working process. Laser forming repairing (LFR) is a promising technique to repair these damaged blades. Unfortunately, the laser formed Ni-based superalloys with high content of (Al + Ti) have a high cracking sensitivity. In this paper, the crack characterization of the LFRed K417G, the microstructure, microhardness and tribological properties of the coating before and after laser remelting are presented. The results show that the microstructure of as-deposited K417G consists of γ phase, γ' precipitated phase, γ+ γ' eutectic and carbide. Cracking mechanisms including solidification cracking, liquation cracking and ductility dip cracking are proposed based on the composition of K417G and processing characteristics to explain the cracking behavior of the K417G superalloy during LFR. After laser remelting, the microstructure of the coating has been refined, and the microhardness and tribological properties has been improved. Laser remelting can decrease the size of the cracks in the LFRed K417G but not the number. Therefore, laser remelting can be applied as an effective method for strengthening coating and as an auxiliary method for controlling cracking.

Keywords: K417G Ni-based superalloy; laser forming repairing; laser remelting; microstructure; cracking behavior; tribology

1. Introduction

Because of the objective reality of enhancing aeroengine performance, blades must work in an environment of high temperature, overloading and high frequency vibration [1]. Ni-based superalloy K417G containing high content of Al + Ti (>7.0 wt. %) is widely used in aeroengine turbine blade for its excellent high-temperature properties and relatively low fabricating cost [2-4]. However, the aeroengine rotor blade zigzag crown appears early failure frequently, which is because of the wear problems occurring in the working process [1]. From efficient and economic point of view, it is more appealing and significant to repair the defected or damaged blades instead of replacing them with new ones. Laser forming repairing (LFR), as same as laser cladding, is a kind of metal additive manufacturing technology. It can be applied to form a repaired coating which

Peer-reviewed version available at *Coatings* **2019**, *9*, 71; doi:10.3390/coatings9020071

recover complex or various defected parts up to certain degree and to form a metallurgical bond between substrate and coating, without degrading the inherent service properties of the parts [5-7].

Unfortunately, cracking behavior frequently occurs when laser rapid forming technology is used to manufacture nickel-based superalloy containing high content of Al + Ti (>7.0 wt. %), which is the most harmful defect that seriously affects the reliability of an aeroengine. Consequently, it is significant to explore the cracking mechanism of nickel-based superalloy and seek control methods of cracking behavior. Ojo and Chaturvedi deemed that the constitutional liquation of γ'phase was the main factor in liquation cracks in Inconel 738 welding process [8,9]. Similarly, Li et al. repaired the damaged K465 superalloy turbine blades by LFR and came to the conclusion that the constitutional liquation of γ' phase resulted in the formation of liquation films during the K465 repairing process [10]. Tancret et al. computed the liquated γ' phase temperature of Inconel 738 by Thermo-Calc software and analyzed the relationship between the heating rate and the dissolution behavior of γ' phase [11]. Zhou and Li et al. pointed out that low melting point phases at grain boundaries such as γ+γ' eutectics and carbides were the main factors in the cracking behavior in K3 nickel-based superalloy during laser cladding [12,13]. Yang et al. manufactured the Rene 104 superalloy by laser rapid forming, found that the cracking sensitivity closely depended on the heat input during forming process, and proposed three cracking mechanisms according to the composition of Rene 104 and different thermal cycle [14].

Although some literatures have investigated the cracking mechanism and laser formed ability of Ni-based superalloy, limited works have been carried out on laser formed K417G superalloy. So far, the microstructure and properties of laser formed K417G, the cracking mechanism and control methods of cracking behavior are still unclear. Moreover, except for component factors and processing parameters, another approach to affect the cracking behavior is post treatment. Laser remelting is considered as an effective post treatment to improve the quality and properties of coating. It has been extensively adopted to prepare coatings with dense structure and excellent properties [15-19]. Therefore, laser remelting can be attempted to decrease or even eliminate the cracks in the LFRed K417G coating. In this paper, the microstructure observation and crack analysis of the LFRed K417G coating are presented. Then cracking mechanisms are proposed taking the chemical composition of K417G superalloy and laser processing characteristics of LFR into account. Finally, the effects on microstructure, cracking behavior, hardness and tribological properties of the LFRed K417G coating after laser remelting are investigated.

2. Materials and Methods

The substrate used in this experiment was the as-cast K417G superalloy with dimensions of ø 25 mm × 8 mm. The K417G spherical powder was supplied by Institute of Metal Research of Chinese Academy of Sciences and refined by gas atomization method. The particle size of powder is 50~150μm and its specific elemental composition is 0.14C, 9.84Cr, 6.37Al, 4.79Ti, 11.4Co, 3.18Mo, 2.80Fe, and balance Ni (wt. %). The laser equipment used in this experiment was a laser direct deposition forming system (Key Laboratory for Anisotropy and Texture of Materials, Ministry of Education, Shenyang, China), which mainly consisted of YAG-1000W fiber laser, protective atmosphere device, and self-designed coaxial ring powder feeding device, circulating cooling device and computer system for forming control. In the laser repairing process, the positive defocusing modes was adopted to obtain a smaller dilution ratio and a higher cladding efficiency, the defocus amount was 4mm, and the spot diameter was 1.8mm. High purity argon (99.99%) was used as the bath protection gas to prevent oxidation, and the shielding gas flow rate was 7L/min. The LFR process parameters of each layer are shown in Table 1 and the schematic of laser scanning path is shown in Figure 1. The laser remelting process parameters were the same as the repair process, except that no powder was fed. The LFRed and remelted coatings were 10 layers in order to ensure adequate thickness. Before and after remelting process, the thicknesses of the coatings were similar, both about 3.8 mm.

Table 1. Main process parameters of laser forming repairing.

Laser power (W)	Scanning speed (mm/s)	Powder feeding amount (g/min)	Powder flow (L/min)	Overlap rate (%)	Z-axis lift (mm)	Interlayer cooling time (min)
600	5.4	5	3.5	40	0.4	10

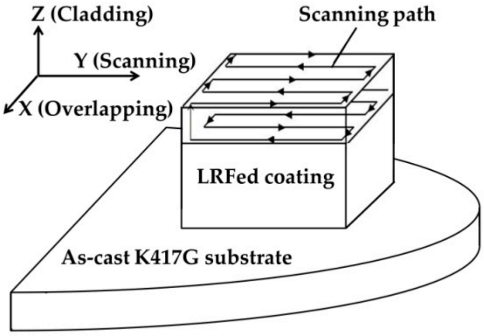

Figure 1. The schematic of laser scanning path.

After preparing, the LFRed coatings were cut into reasonable size blocks together with the substrate by numerically controlled wire-cutting. After being mechanically ground and polished, the sectioned samples were electrolytically etched in 15g CrO3 + 10ml H2SO4 + 150ml H3PO4 at 5V for 35-50s. Samples were ultrasonically cleaned after corrosion for 10min, and finally rinsed with absolute ethanol and dried. The phase composition was measured using an X-ray diffractometer (XRD) (Smartlab-9000, Rigaku, Tokyo, Japan) machine and the main operating parameters included a 40 kV voltage, 250 mA current, Cu Kα radiation, 0.02° angle step-length, and 5°/min scanning rate. Scanning electron microscope (SEM) (JSM-6510A, JEOL, Tokyo, Japan) and its own energy spectrum analyzer (EDS) were used by microstructure observation, micro-area composition analysis and wear surface analysis of samples. The dendritic spacing and cracking size were measured by Image-Pro Plus 6.0 image analysis software (Image-Pro Plus software, Media Cybernetics, Bethesda, MD, USA). The microhardness was measured by digital micro vickers hardness tester (401MVD, Wolpert Wilson, Norwood, USA). The test areas were regions from the top of the coating to the substrate in the longitudinal section of Y-Z. A load of 200 g was applied, and the holding time was 10 s. The hardness test for each sample was in three times, and the average of three datas was taken as the microhardness of the samples. Tribological properties of samples were evaluated using Universal friction and wear tester (Nanovea, Irvine, USA) and its own 3D contact surface profiler. The samples with dimensions of ø 15 mm × 10 mm were prepared to conduct the wear experiment at room temperature. The radius of the wear tracks was set to 3 mm using φ6 mm Si3N4 balls as a counterpart. The measurements were implemented for a sliding length of 54 m with a speed of 15mm/s, a load of 10 N and a relative humidity of 60% ± 3%.

3. Results and Discussion

3.1. Microstructure and Main Phases of LFRed K417G Superalloy

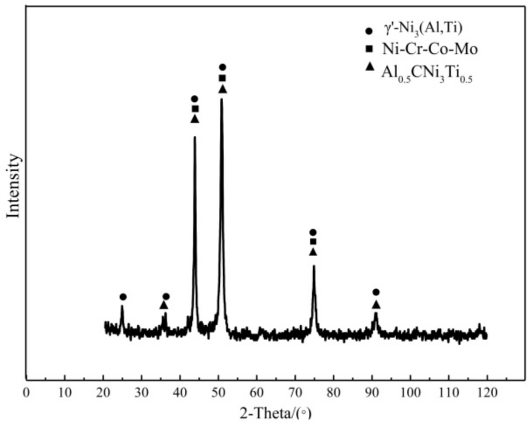

Figure 2. XRD diffraction pattern of the LFRed K417G.

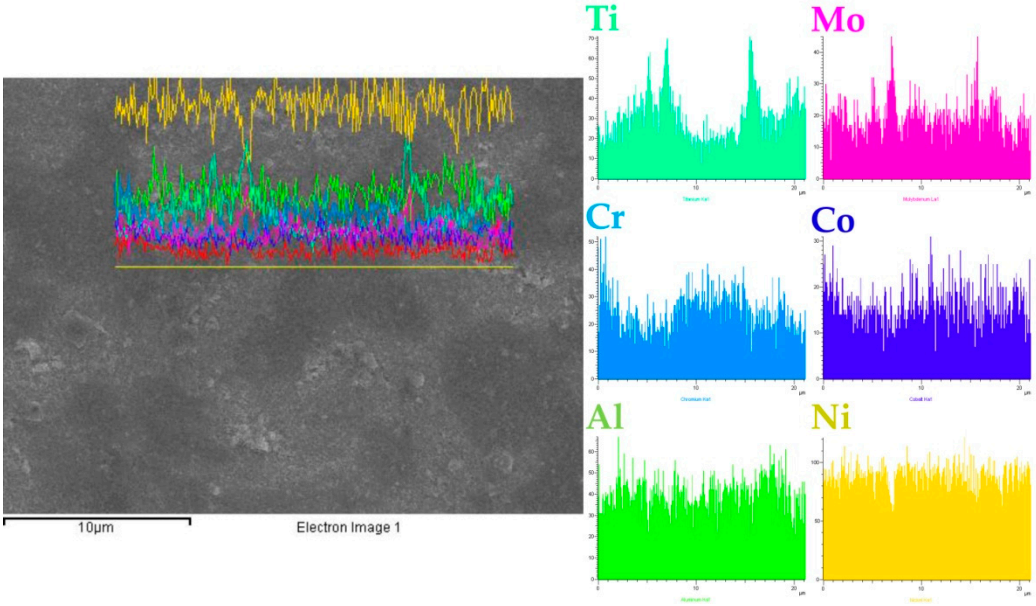

Figure 3. Energy dispersive spectrometer (EDS) results of line scanning on the X-Y section.

Samples are examined in order to determine the phase composition using an X-ray diffraction analyzer (XRD). Figure 2 is an XRD diffraction pattern of the LFRed K417G superalloy coating. It can be seen that the coating mainly contains γ solid solution rich in matrix elements such as Cr, Ni, Co, and Mo, Al0.5CNi3Ti0.5 carbide and γ′-Ni3(Al, Ti) strengthening precipitation phase. Figure 3 shows the SEM microstructure and the EDS analysis results of line scanning on the X-Y section. The results indicate that Ti and Mo elements are significantly segregated between the dendrites, while Cr and Co are evenly distributed in the dendrites. Figure 4 shows a typical microstructure on the X-Z section. The darker areas in Figure 4a are dendrites, while the brighter areas are interdendritic zones, the measured dendrite spacing is 10～18μm. There are mainly three types of precipitates between dendrites which are finely distributed dot-like precipitates, white block-shaped precipitates and gray-white fishbone-like tissue. The proportion of white block-shaped precipitates and gray-white fishbone-like tissue are higher, occupying half of the interdendritic zones and distributing nonuniformly.

Peer-reviewed version available at *Coatings* **2019**, *9*, 71; doi:10.3390/coatings9020071

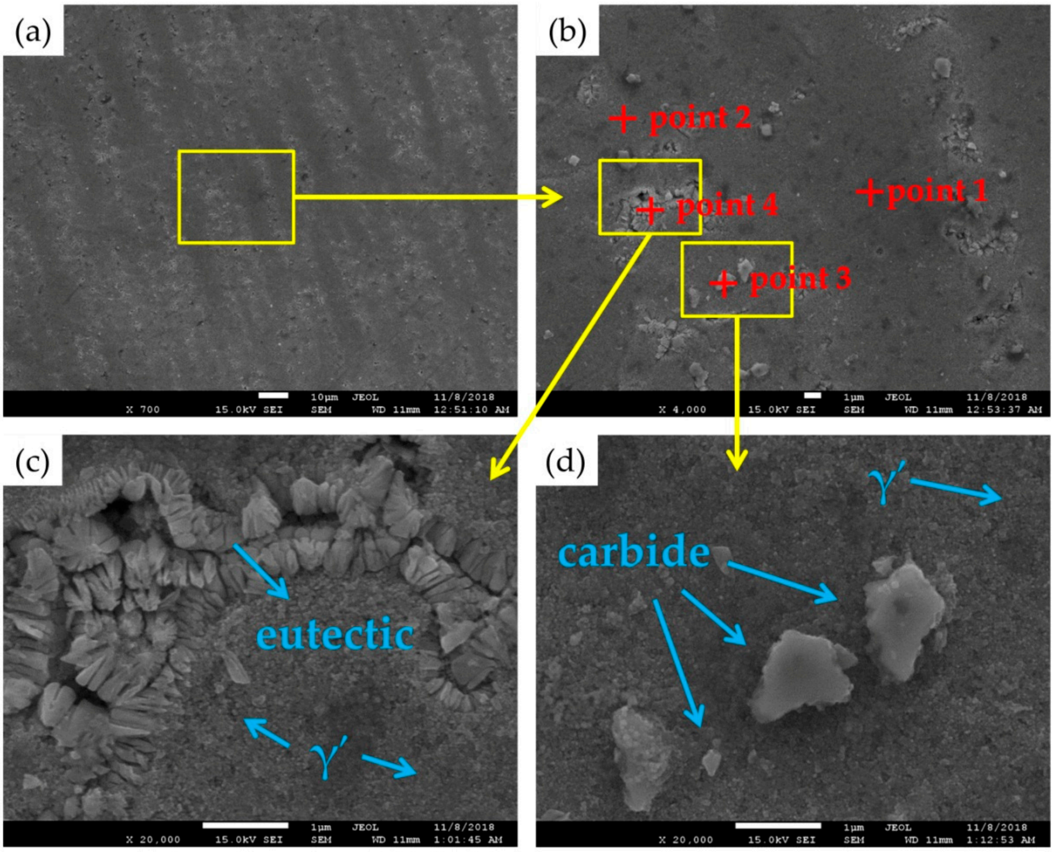

Figure 4. Typical microstructure on the X-Z section of the LFRed K417G.

Table 2. Elements concentration of different test points (mass fraction %).

	C	Al	Ti	Cr	Fe	Ni	Mo	Co
Point 1	1.79	4.65	1.91	9.33	7.87	62.34	2.81	9.45
Point 2	2.61	5.85	7.36	5.73	2.46	64.13	4.62	3.52
Point 3	8.72	5.56	6.24	9.23	5.62	51.23	3.20	5.72
Point 4	3.87	3.52	6.03	7.52	3.16	61.25	3.23	5.26
Powders	0.14	6.37	4.79	9.84	2.80	61.2	3.18	11.4

In order to further analyze the microstructure and phase composition, energy dispersive spectrometer (EDS) of point scanning is performed on typical locations on the microstructure. As shown in Table 2, the results indicate that the composition of dark-gray zone in dendrites (point 1 in Figure 4b) is similar to that of the original powder, while the contents of Al, Ti and Mo are lower than the original powder. This is because during the solidification process, since the laser deposition is a near-rapid cooling process, the Al, Ti and Mo element will be segregated in the remaining liquid phase during the non-equilibrium solidification process and finally solidified. Therefore, the dark-gray zone (point 1 in Figure 4b) is γ matrix phase. The element distribution of finely distributed dot-like precipitates between dendrites (point 2 in Figure 4b) is close to that of the matrix, but the content of Al and Ti is increased. Combined with the previous XRD results and morphological comparison of precipitates in some literatures on Ni-based superalloys [20,21], it can be concluded that the location of point 2 is the γ phase plus γ' phase Ni3(Al, Ti), in addition, the aggregation of Ti will make the γ' phase coarse. The location of point 3(in Figure 4b) shows the white block-shaped precipitates distributed between dendrites. Elemental analysis shows that the C, Ti and Mo elements are enriched in the particle precipitated phase compared with the matrix phase. Its morphology is characterized by MC-type carbides, where M represents the metal elements Al, Ti and Mo. According to previous XRD analysis, it is presumed that the precipitation form of MC should be (Al,

Peer-reviewed version available at Coatings 2019, 9, 71; doi:10.3390/coatings9020071

Ti, Mo) C. However, considering some types of carbides such as M6C, M23C6, etc. are usually hard to detect in XRD, it is difficult to determine whether other types of carbides are present in LFRed K417G superalloy coating [21,22]. The content of elemental composition at point 4 is similar to that at point 2. The contents of C and Ti are slightly higher, and the form is clustered or fishbone. This is $\gamma+\gamma'$ eutectic structure. The matrix is first formed during solidification, Al and Ti elements are segregated in the liquid to precipitate and grow the γ' phase in advance, finally the remaining liquid is pushed to the interdendritic position to cause eutectic reaction at a lower temperature, then eutectic structure forms [21,23-26].

3.2. Cracking Behavior and Mechanisms of LFRed K417G Superalloy

3.2.1. Crack Observation and Analysis

Unfortunately, severe cracking behavior occurs in the LFRed K417G samples. Figure 5a shows the cracks on X-Z section, it can be found that cracks with the length in the range of 0.2mm to 2 mm existing in the repair zone (RZ) and the heat affected zone (HAZ). In addition, the cracsks are always parallel to the depositional direction, have the same orientation as the columnar crystal. This is because the grain boundary is considered as a favorable crack initiation site, so that cracks tend to form along the grain boundary except a few initial points in the pores, which is similar to the results presented by Carter et al [27]. In addition, crack count and density defined as the total number of cracks per unit area by Ghosh and Partha are measured to estimate the cracking sensitivity [28]. Figure 5b gives crack count and density of the LFRed samples. According to the observation of sections and the statistical results in Figure 5, it can be concluded that compared with most of superalloys, the cracking sensitivity of as-deposited K417G is more serious [8-14,29].

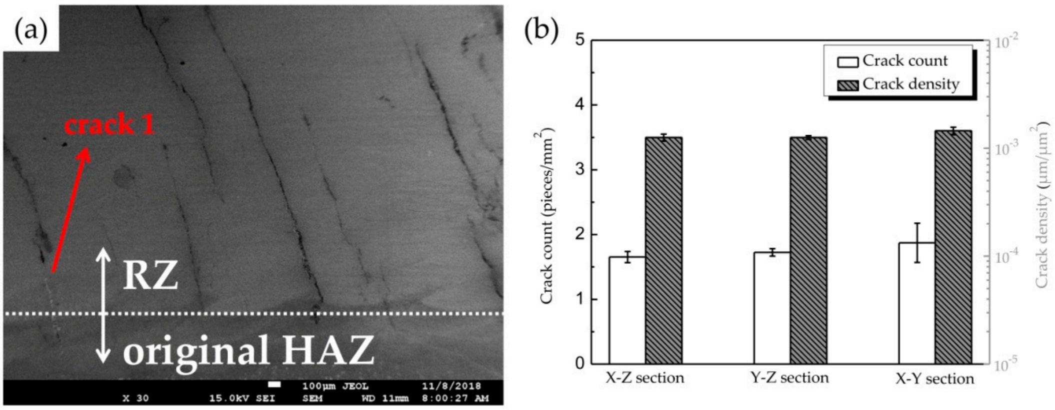

Figure 5. (a) The cracks on X-Z section and (b) crack count and density on three sections of LFRed K417G coating.

This characteristic of cracking behavior is mainly influenced by the composition of K417G and the processing of LFR. Firstly, K417G has a very high content of Al and Ti (11 wt.%) which are γ'-Ni3(Al, Ti) forming elements. Consequently, a large amount of γ' phase exists in the K417G superalloy. On one hand, these γ' phase play the role of stapling dislocation and thus strengthen the alloy. On the other hand, The contraction stresses during the precipitation of γ'-Ni3(Al, Ti) and the forming of low melting point (γ + γ') eutectics will be caused by these γ' phase, which will dramatically increase the cracking sensitivity of the alloy.[22,30] Secondly, the processing characteristic of LFR is another vital factor to affect the cracking sensitivity. LFR is a process of layer-by-layer superposition. Deposited layers of different heights undergo different thermal cycles. During LFR, when the laser focuses a certain location, the powder at there is heated and rapidly melted. As the laser moves away, the melted material at this location cools rapidly. The material at this location will undergo a complex cycle of repeated heating or even remelting as the next layer of cladding takes place. In fact, any position within the LFRed coating, except for the final

Peer-reviewed version available at *Coatings* **2019**, *9*, 71; doi:10.3390/coatings9020071

solidification areas on the top, will follow this cycle. This process of repeatedly rapid heating and cooling carries a high risk of cracking [31,32].

3.2.2. Cracking Mechanisms

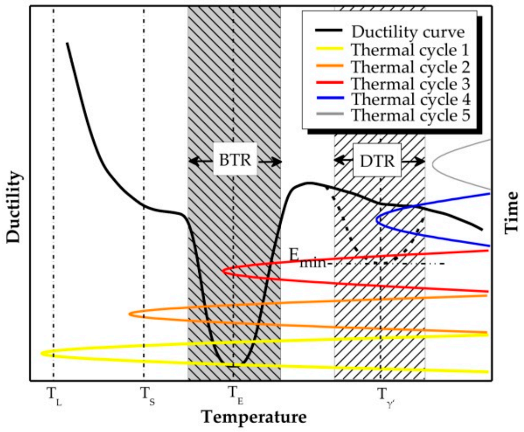

Figure 6. Schematic diagram of the combined effect of ductility curve and thermal cycle.

In order to further explore the influence of composition and process on cracking sensitivity of LFRed K417G, a schematic diagram of the combined effect of ductility curve and thermal cycle is drawn. As shown in Figure 6, the ductility of the material changes as the temperature decreases in the solidification process. There are two regions with obviously low ductility. One is the brittleness temperature region (BTR), which is prone to solidification cracking (SC) and liquation cracking (LC). The other is the ductility dip temperature region (DTR), which is prone to ductility dip cracking (DDC). The two low ductility regions are around the temperature of eutectic reaction temperature (TE) and (Tγ') respectively. While around other temperature of liquidus temperature (TL) and solidus temperature (TS) show no low ductility regions. In addition, it can be found from Figure 6 that material will undergo five types of thermal cycles which peak temperature is respectively above TL, above T_S, above T_E, above Tγ', and below Tγ'. The time of each thermal cycle is related to the process of LFR while the ductility curve is mainly related to the composition of superalloy. When the thermal cycle of the material is in two regions of BTR and DTR, the cracking behavior will be generated. Therefore, it can be inferred that there are three types of cracking behavior which respectively are solidification cracking, liquation cracking and ductility dip cracking in LFRed K417G superalloy.

3.2.2.1. Solidification Cracking

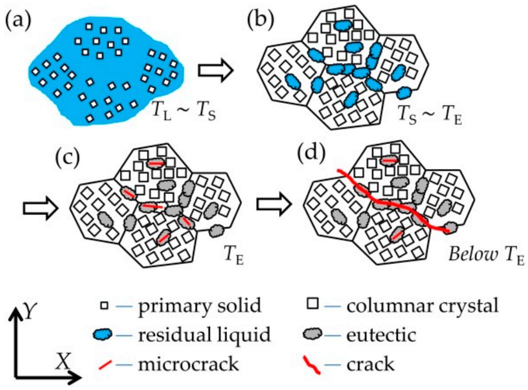

Figure 7. Schematic diagram of the formation process of solidification cracking.

Figure 7 shows the formation process of solidification cracking. When the temperature drops below TL, the primary solid phase of different orientations begins to form. When the temperature drops below TS, these different orientations of solids grow alternately to form the dendrite skeleton.

Peer-reviewed version available at *Coatings* **2019**, *9*, 71; doi:10.3390/coatings9020071

In this case, the grain boundary cannot move or rotate relatively, nor can the residual liquid phase flow freely between the solid dendrites, forming a closed and continuously distributed liquid film between the dendrites. Moreover, the rapid cooling rate results in the non-equilibrium solidification and enrichment of Al and Ti in the interdendritic zones. When the content of (Al + Ti) in the liquid phase reaches the critical value, the eutectic reaction of $L \rightarrow \gamma + \gamma'$ will be generated between the dendrites, thus the eutectic structure forming. At this time, the temperature is TE. Under the action of contraction stress, continuous liquid film ends produce strain concentration, and at this time, the deformation of the alloy can only be achieved by the deformation or bending of dendrites. The deformation resistance is large, and it is easy to separate between grains and crack in the weak eutectic structure between grains. In the process of continuous solidification (below the temperature of TE), the microcrack propagates along the brittle intercrystalline, thus forming the solidification crack. This cracking process is during the thermal cycles of 1 and 2 (the yellow line and orange line in Figure 6).

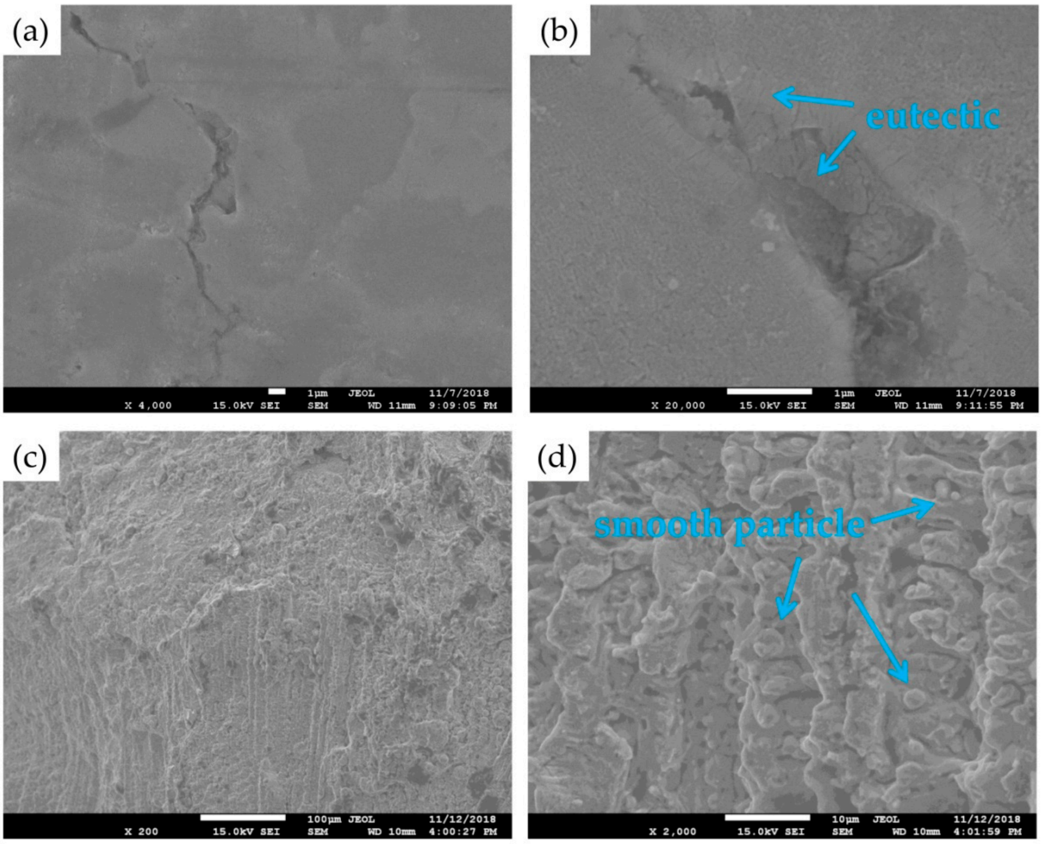

Figure 8. Morphology of (a) (b) a solidification crack and (c) (d)its section.

In the process of crack growth, the residual stress is gradually released and the energy required for crack growth is gradually reduced. At the same time, as the sediment layer in the extension zone has solidified, the closer to the substrate, the more completely solidified, and the strength of intercrystalline bond is greater. When the stress is not enough to break the intercrystalline bond, the crack will be terminated. In addition, as the number of sedimentary layers increases, the tensile stress in the repaired area gradually decreases and changes to compressive stress, and the crack expansion along the sedimentary direction towards the top will be impeded. Therefore, most of solidification cracks will appear perpendicular to the direction of deposition and most of them will be on the top of the LFRed coating. Figure 8c and d shows the morphology of the smooth area of the crack section, where there are almost no holes in the depth direction, which is determined by the nearly two-dimensional distribution of the interdendritic liquid film. Because the cracking is carried out along the liquid film of between the dendrites, the dendrites remain free in

Peer-reviewed version available at Coatings 2019, 9, 71; doi:10.3390/coatings9020071

the liquid phase and appear as round grains with smooth surface. Consequently, it can be seen that the crack in Figure 8a belongs to solidification crack.

3.2.2.2. Liquation Cracking

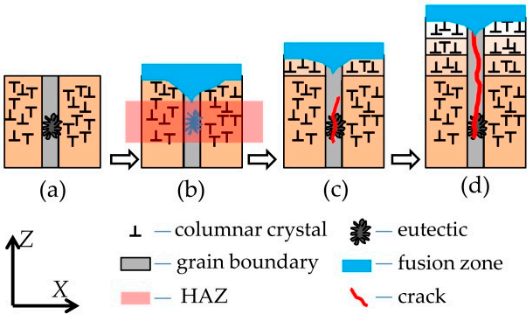

Figure 9. Schematic diagram of the formation process of liquation cracking.

Liquation cracking is the most common form of cracking behavior in superalloys with high (Al+ Ti) content. Unlike solidification cracking, the source of liquation cracking is low-melting point eutectics in the heat affected zone (HAZ). These solidified eutectics will be re-melted to form liquid film when the reheated temperature is above TE, which will lead to intergranular cracking under the action of contraction force. This cracking process is during the thermal cycles of 3 (the red line Figure 6). Figure 9 shows the formation process of liquation cracking. It is worth noting that HAZ does not only exist in the substrate, but also exist in the previous layer when laser is focusing on current layer. In other words, there are countless HAZ inside the coating as long as the laser melting is not performed only once. To be exact, the HAZ shown in Figure 5 is only the original HAZ. With the continuous progress of LFR process, HAZs are constantly formed, and the eutectics with low-melting point in HAZs are constantly remelted, thus forming more and more crack sources. Due to the characteristic of epitaxial growth on the structure during LFR process, the structure between layers and layers has genetic characteristic, which is easy to form columnar crystals with strong directivity. Consequently, the channels through the columnar dendrites between layers are generated. Once the liquefied microcrack is formed at the grain boundary, it will expand along the grain boundary with the accumulation of residual tensile stress and form the macroscopic crack through many deposited layers. The crack propagation requires more energy to be prevented, unless the steering dendrite with greater directional variation or the equiaxed grain is encountered.

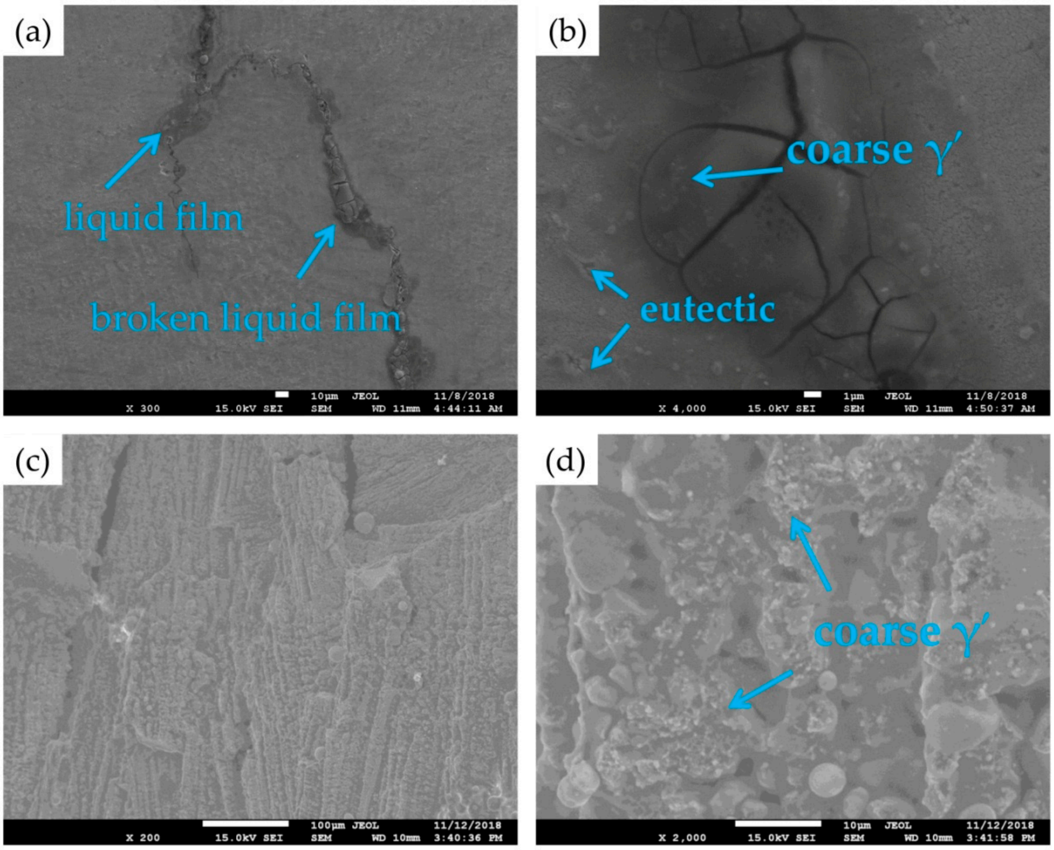

Figure 10. Morphology of (a) (b) a liquation crack and (c) (d)its section..

Liquation cracks usually grow along the direction of dendrite growth, which is similar to an upward growth direction parallel to deposition. As shown in Figure 10a, the extension direction of the crack seems to follow the growth law above. Moreover, it can be seen from Figure 10b that the crack is filled with broken liquid film, and eutectic and coarse γ′ are distributed around the crack. Figure 10c shows the macroscopic morphology of the crack section. It has the characteristic of intergranular cracking. The microscopic morphology of crack section (in Figure 10d) shows that the grain boundary surface is rather round with dendritic protrusions, and obvious liquation of dendrite protrusions can be observed. Therefore, the crack section takes on the shape of potato in different sizes, indicating that it is the result of interdendritic liquid film separation and is a typical liquation crack. However, for the judgment of cracking mechanism of other cracks in Figure 5a, it is not sufficient to observe the growth direction only. Due to the complex solidification process of melting, remelting, partial remelting, cyclic annealing and countless HAZ within the LFRed coating, it is difficult to identify the cracking behavior belongs to the liquation cracking or solidification cracking [33,34]. At least it can be determined that crack 1 in Figure 5a belongs to the liquation crack, as it exists in the original HAZ and is similar to an upward growth direction parallel to deposition.

3.2.2.3. Ductility Dip Cracking

Peer-reviewed version available at *Coatings* **2019**, *9*, 71; doi:10.3390/coatings9020071

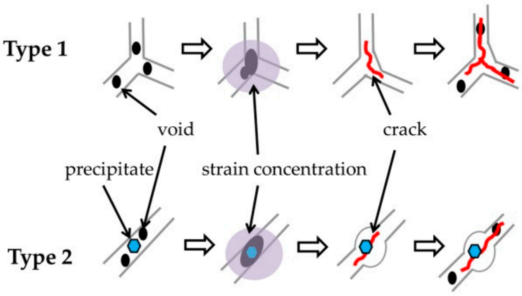

Figure 11. Schematic diagram of the formation process of ductility dip cracking.

When the material is in during the thermal cycle 4 (the blue line Figure 6), it will suffer the effect of continuously growing solid-phase shrinkage stress. No liquid phase exists in this process, and the deformation mode mainly depends on the vacancy diffusion or the dislocation climb along the grain boundary. When the process of diffusion or climb meets obstacles, it will lead to cracking due to strain concentration. At this moment, the crack formed belongs to ductility dip crack. Since these obstacles can be the vertex where the three grains intersect, or the precipitates on the grain boundary, ductility dip cracking is generally generated by two modes, as shown in Figure 11. The straight grain boundaries promote grain boundary sliding to form large voids and corresponding strain concentration at a vertex where the three grains intersect. These voids at the vertex eventually develop into a crack, which is the mode 1 in Figure 11. The mode 2 in Figure 11 is mainly related to the precipitates. In fact, the precipitates play a double role in the effect on the sensitivity of ductility dip cracking. On the one hand, the precipitates lock the grain boundaries and reduce the grain boundary sliding, thus reducing the strain concentration at the vertex of three adjacent grains. These precipitates, on the other hand, lock the grain boundaries but accumulate strain and voids around the precipitates themselves, which may lead to the formation of cracks [35]. The effect of precipitates on the sensitivity of ductility dip cracking depends on the type, size and distribution of precipitates. The situation is very complicated. Emin in Figure 6 is the critical strain value of ductility dip cracking in the DTR, and its value can be used as an indicator to determine the sensitivity of ductility dip cracking of the material. When the precipitates play a role in inhibiting ductility dip cracking, Emin will be slightly below the ductile curve, at which time the width of DTR is very narrow or even does not exist.

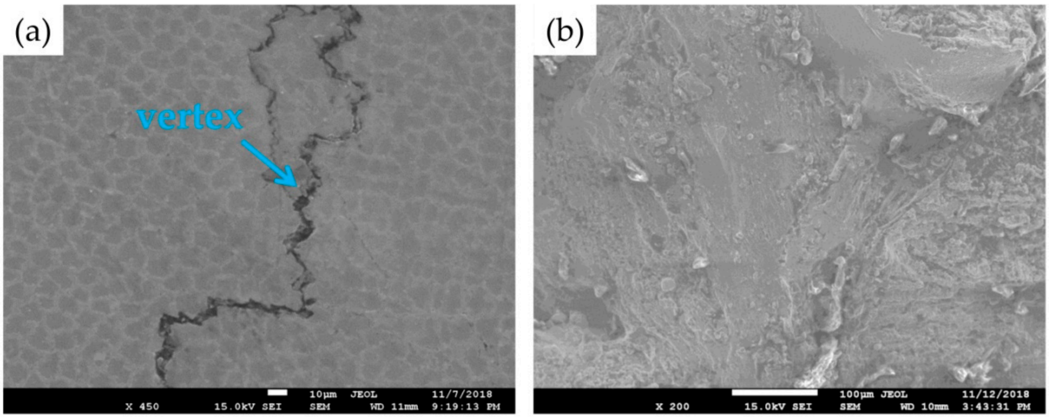

Figure 12. Morphology of (a) a ductility dip crack and (b) its section..

The crack shown in Figure 12a passes through the vertex of the three adjacent grains and extends along the grain boundaries of these three grains. Moreover, the section in Figure 12b shows that no liquid film exists at the grain boundary of this crack. Consequently, it indicates that the crack should be a ductility dip crack formed in the mode 1 in Figure 11. However, since it is difficult to find ductility dip cracks formed in mode 2, and if solidification cracking and grain boundary liquation cracking have occurred, the cracks expansion at this temperature will be further

Peer-reviewed version available at *Coatings* **2019**, *9*, 71; doi:10.3390/coatings9020071

intensified or connect with ductility dip cracks. Therefore, the effect of precipitates on the sensitivity of ductility dip cracking in LFRed K417G is still unclear.

In summary, it can be determined that the cracking mechanism of cracks in LFRed K417G coating is respectively solidification cracking, liquation cracking and ductility dip cracking. However, the judgment of cracking mechanism of a crack requires comprehensive evidence, which should combine with observation of macroscopic and microscopic morphology, determination of composition and analysis of fracture, etc. Moreover, the judgment may still not be completely accurate, since sometimes it may be a combination of multiple cracking mechanisms. Fortunately, all cracking behaviors are related to composition and process. Therefore, adjusting composition, optimizing process parameters and post treatment can be utilized to control or eliminate cracking behavior.

3.3. Effect of Laser Remelting Process on Microstructure and Cracking behavior

3.3.1. Microstructure after Remelting

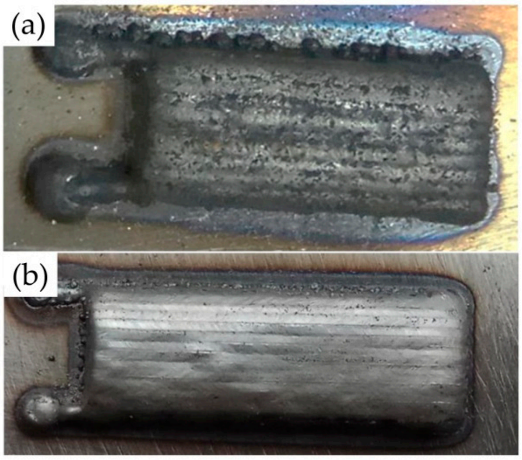

Figure 13. Surface morphology of samples (a) before and (b) after laser remelting.

Laser remelting is considered as an effective post treatment to improve the quality and properties of LRFed K417G coating. As shown in Figure 13, the surface quality of the coating after laser remelting is obviously superior to that before remelting. Laser remelting is also the process of reheating and solidification of the material. No new alloy powder is added during this process. Sharp points and small metal particles can absorb laser energy and remelt. It can be seen that a laser remelting process after laser deposition can make the surface smooth.

Peer-reviewed version available at Coatings 2019, 9, 71; doi:10.3390/coatings9020071

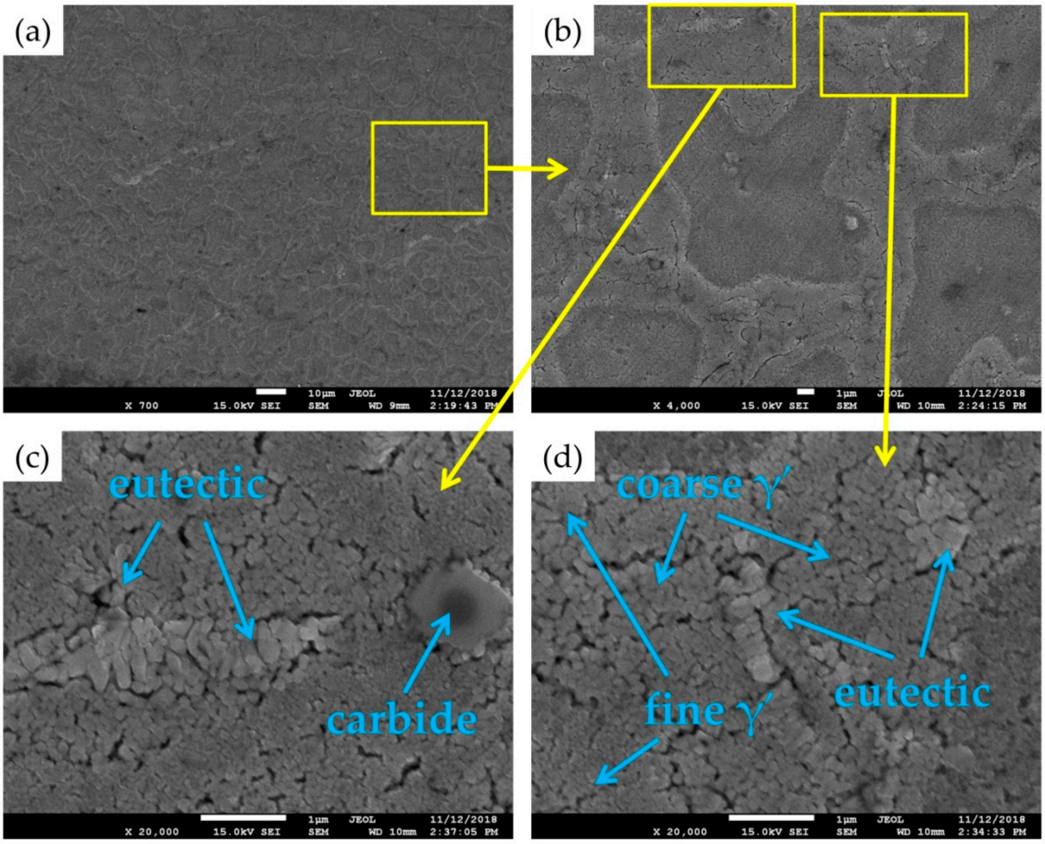

Figure 14. Typical microstructure on the X-Z section of the as-remeltedLFRed K417G.

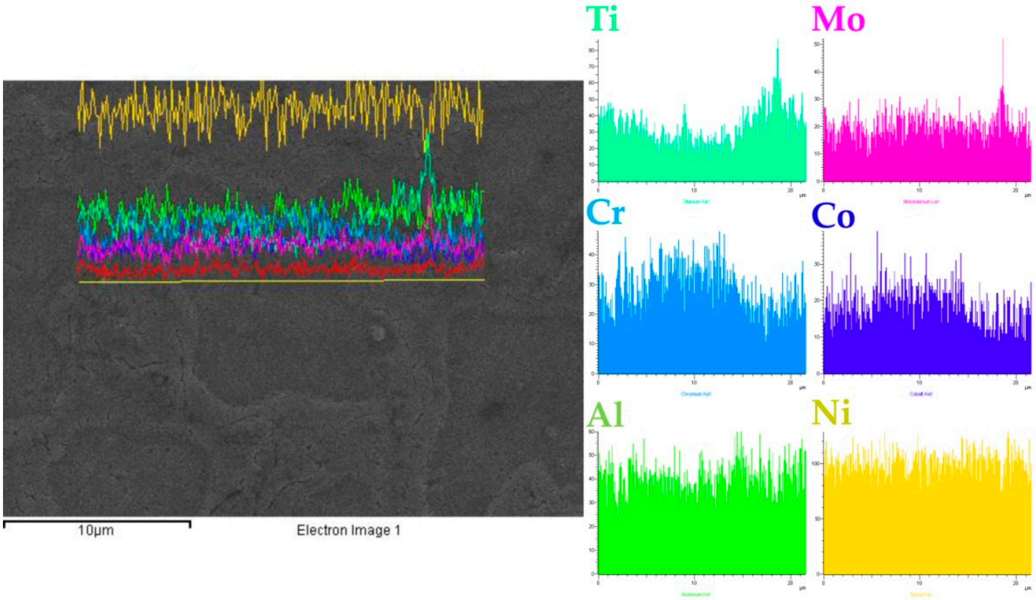

Figure 15. Energy dispersive spectrometer (EDS) results of line scanning in the local zone of Figure 14b.

Figure 14 shows the microstructure of LFRed K417G coating after laser remelting. The microstructure is still mainly composed of γ phase, γ' precipitated phase, γ+ γ' eutectic and carbide. Moreover, γ' also has a large distribution inside the dendrites, rather than almost always precipitating between the dendrites. After remelting, the microstructure is obviously refined, and the size of the precipitate is reduced. It can be seen from the comparison between the line scan results in Figure 15 and Figure 3 that the element segregation is somewhat reduced and the element distribution is more uniform.

3.3.2. Cracking Behavior after Remelting

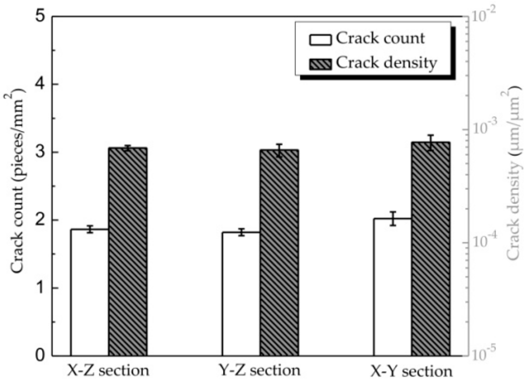

Figure 16. Crack count and density on three sections of as-remelted LFRed K417G.

Figure 16 shows the crack number and crack density of the three sections in the as-remelted K417G coating. From the statistic of the crack count, the number of cracks in the coating after remelting does not decrease, but increases slightly which is undesirable phenomenon. However, the crack density decreases significantly which is already less than 10^{-3} μm/μm^2. This indicates a significant reduction in the size of the cracks in the coating. Combined with the analysis of section 3.2.2, it can be speculated that laser remelting plays a double role in cracking behavior. On the one hand, due to the effect of rapid heating and rapid solidification in the process of LFR, the material has experienced five types of thermal cycles (in Figure 6), of which four will generate cracks. Laser remelting causes the material to undergo these thermal cycles again, thus doubling the susceptibility of cracking. And the thermal stress is higher because of the heat input again. On the other hand, laser remelting refines the microstructure, reduces elemental segregation, makes the precipitates more evenly distributed, and creates grains with more different orientation, which will undoubtedly hinder the connection of liquid film, thus hindering the extension of microcracks. For large cracks, especially the liquation cracks that have already formed in the HAZ, laser remelting is difficult to heal, and these cracks will become larger due to higher thermal stress. As a result of this double action, the cracks continue to expand, the number of medium size cracks decreases and the number of small size cracks increases.

3.4. Effect of Laser Remelting Process on Microhardness and Tribological Properties

3.4.1. Microhardness

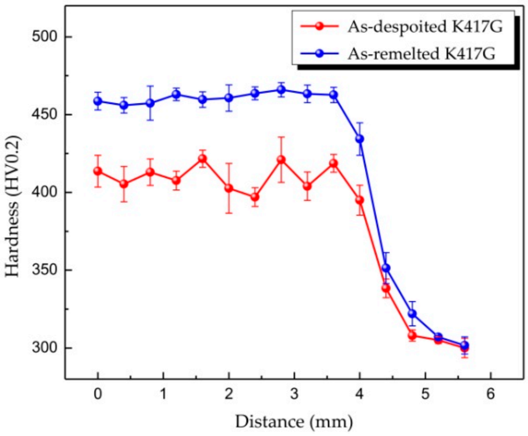

Figure 17. Microhardness of the LFRed K417G before and after laser remelting.

Figure 17 shows the microhardness of the LFRed K417G coating before and after laser remelting process, from which it can be seen that the as-remelted coating has higher microhardness than that in as-deposited coating, and the increase is about 50HV0.2. Moreover, the microhardness of the as-deposited coating changes unsteadily, while the hardness distribution and the dispersion of each measuring point in the as-remelted coating are more uniform. According to the results discussed in section 3.3, the microstructure after laser remelting is more refined, the distribution of precipitates is more uniform, the size and number of γ+γ′ eutectics which are harmful to the improvement of hardness are reduced, and more γ′ are distributed in dendrites, which has a more significant enhancement effect. These combined effects result in hardness improvement and uniform distribution.

3.4.2. Tribological Properties

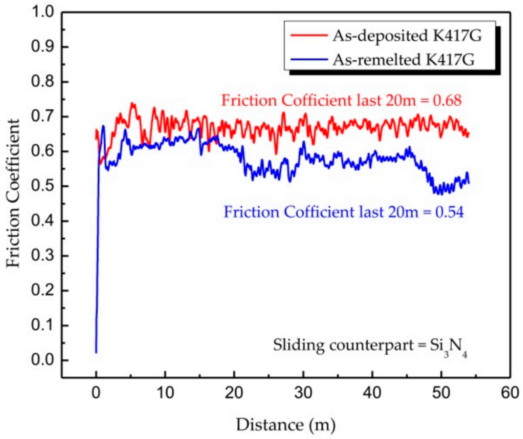

Figure 18. The friction coefficient of the LFRed coatings before and after laser remelting process.

Friction coefficient evolutions of as-deposited K417G and as-remelted K417G are shown in Figure 18. The raw data has been smoothed (10 points Savitzky–Golay smooth) to facilitate the analysis of the results. At the beginning of the test, the friction coefficients of the two samples reach a high value. This indicates that the friction surface begins to show plastic deformation and adhesion since the beginning of the test, and under the effect of shear stress, the particles begin to peel off on the surface of the material. The average values of friction coefficients in the final 50 m sliding of the as-deposited and as-remelted samples are 0.68 and 0.54, respectively. It's worth noting that this friction coefficient is not a steady state value. Because at the end of the test, the two samples cannot reach the steady state, there are still large fluctuations. In general, the friction coefficient of as-remelted sample is less than that of as-deposited sample. Moreover, the friction coefficient of as-remelted sample shows a downward trend in the late test period, while the as-deposited sample still fluctuates within a larger value.

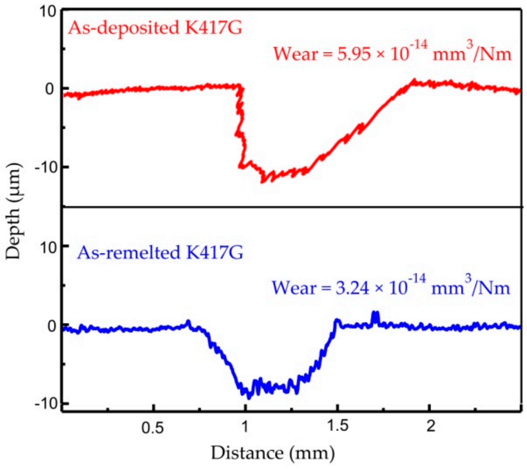

Figure 19. The 2D profiles of the wear track of the as-deposited K417G and as-remelted K417G tested against Si3N4 balls.

As shown in Figure 19, two-dimensional profiles of the wear tracks are obtained at the end of tests. The raw data has been smoothed (10 points Savitzky–Golay smooth) as well. The result clearly shows that, after 54 m of sliding, the depth and width of the wear tracks are much larger for as-deposited K417G than for the as-remelted K417G. The wear rates of the as-deposited K417G and the as-remelted K417G are 5.95 ×10-14mm3/Nm and 3.24 ×10-14mm3, respectively. The wear rate of the coatings agrees well with the expected inverse proportional relation between this property and the hardness of the coatings. All these show that the as-remelted K417G has better tribological properties.

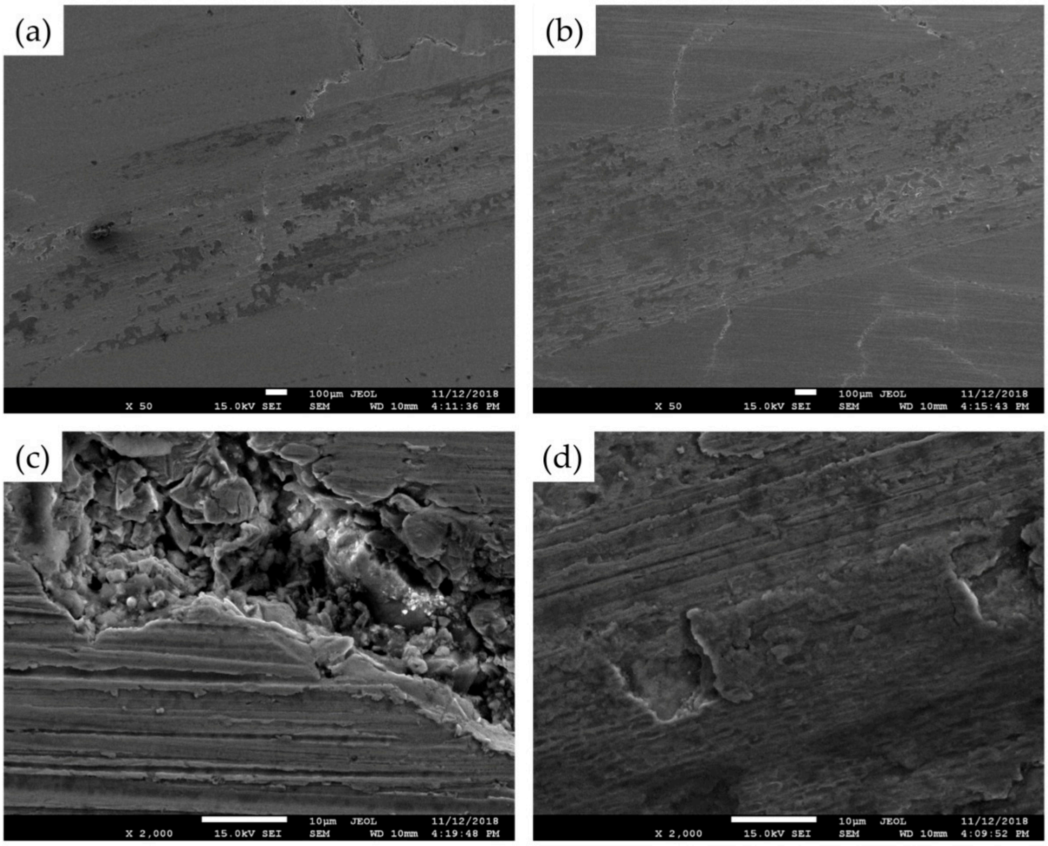

Figure 20. Wear surfaces of (a) (c) the as-deposited K417G and (b) (d) the as-remelted K417G.

Figure 20 shows the wear surfaces of the as-deposited K417G and the as-remelted K417G. The two wear surfaces both are similar to the form of adhesion wear surface. Large areas of peeling and oxidation can be seen on the wear surfaces. As can be seen from Figure 20c and d, both wear surfaces have deep scratches. These scratches are not similar to those caused by abrasive particles. They are more likely to be caused by scraping of the abrasive chip that has flaked and adhered to the surface. In addition, it can be observed that the cracks on the surface of the as-remelted K417G will be separated by the wear surface, while the crack on the surface of the as-deposited K417G will pass through the wear surface, showing that the cracks in the as-remelted K417G are shallower. This confirms, from another aspect, the effect of laser remelting on the reduction of crack size as discussed in section 3.3.2.

4. Conclusions

The K417G Ni-based superalloy has been prepared on as-cast K417G substrate by LFR process. Laser remelting process has applied as a post treatment to improve the properties of the LFRed coating. The main conclusions are as follows.

The microstructure of the LFRed K417G consists of γ phase, γ' precipitated phase, γ+ γ' eutectic and carbide. The characteristic of cracking behavior is mainly influenced by the composition of K417G and the processing of LFR. Cracking mechanisms of the LFRed K417G include solidification cracking, liquation cracking and ductility dip cracking.

Laser remelting can decrease the size of the cracks in the LFRed K417G but not the number. After laser remelting, the microstructure of the coating has been refined, and the element segregation has been reduced. The as-remelted coating has higher microhardness which can reach up to 460 HV0.2 than that in as-deposited coating, and the increase is about 50HV0.2. Similarly, the as-remelted K417 has better tribological property than the as-deposited K417G. The wear surfaces both are related to adhesion wear.

Consequently, in the application of LFR technology to repair damaged K417G blades, laser remelting can be applied as an effective method for strengthening coating and as an auxiliary method for controlling cracking. However, cracks still exist. In order to eliminate cracking behavior, more efforts should be committed to component adjustment, process parameter optimization and other post-treatment studies.

Author Contributions: Changsheng Liu conceived the experiments and provided experimental conditions; Jinguo Li provided K417G master superalloy; Suiyuan Chen prepared K417G powder; Yang Wang and Haixin Yu prepared the samples; Haixin Yu and Shuai Liu performed the performance tests; Xue Zhang and Shuai Liu analyzed the data; Shuai Liu wrote the paper.

Funding: This research was funded by the Joint Founds of National Natural Science Foundation of China (NSFC)-Liaoning (No.U1508213) and National Key Research Project (No. 2017YFB0305801).

Acknowledgments: This work was supported financially by the The work was supported by the program for the Joint Founds of National Natural Science Foundation of China (NSFC)-Liaoning (No.U1508213) and National Key Research Project (No. 2017YFB0305801). Bin Zhang and Jing Liang from Northeastern University are gratefully acknowledged for data analysis.

Conflicts of Interest: The authors declare no conflict of interest.

Abbreviations

The following abbreviations are used in this manuscript:

LFR	Laser Forming Repairing
LFRed	Laser Forming Repaired
HAZ	Heat Affected Zone
RZ	Repaired Zone

Peer-reviewed version available at *Coatings* **2019**, *9*, 71; doi:10.3390/coatings9020071

References

1. Koh, K.H.; Griffin, J. H.; Filippi, S.; Akay, A. Characterization of turbine blade friction dampers. *J. Eng. Gas Turbines Power* **2004**, *127*, 856-862, 10.1115/1.1926312.
2. Yang, C.X.; Xu, Y.L.; Nie, H.; Xiao, X.S. ; Jia, G.Q.; Shen, Z. Effects of heat treatments on the microstructure and mechanical properties of Rene 80. *Mater. Des.* **2013**, *43*, 66–73, 10.1016/j.matdes.2012.06.039.
3. Yang, Y.H.; Xie, Y.J.; Wang, M.S.; Ye, W. Microstructure and tensile properties of nickel-based superalloy K417G bonded using transient liquid-phase infiltration. *Mater. Des.* **2013**, *51*, 141–147, 10.1016/j.matdes.2013.04.024.
4. Du, B.N.; Yang, J.X.; Cui, C.Y.; Sun, X.F. Effects of grain refinement on the microstructure and tensile behavior of K417G superalloy. *Mater. Sci. Eng. A* **2015**, *623*, 59–67, 10.1016/j.msea.2014.11.041.
5. Gaumann, M.; Henry, S.; Cleton, F.; Wegniere, J.D.; Kurz, W. Epitaxial laser metal forming: analysis of microstructure formation. *Mater. Sci. Eng. A* **1999**, *271*, 232–241, 10.1016/S0921-5093(99)00202-6.
6. Lin, X.; Yue, T.M.; Yang, H.O.; Huang, W.D. Microstructure and phase evolution in laser rapid forming of a functionally graded Ti–Rene88DT Alloy. *Acta Mater.* **2006**, *54*, 1901–1915, 10.1016/j.actamat.2005.12.019
7. Liu, F.C.; Lin, X.; Huang, C.P.; Song, M.H.; Yang, G.L.; Chen, J.; Huang, W.D. The effect of laser scanning path on microstructures and mechanical properties of laser solid formed Nickel-base superalloy Inconel 718. J. *Alloy. Compd.* **2011**, *205*, 4505–4509, 10.1016/j.jallcom.2010.11.176.
8. Ojo, O.A.; Richards, N.L.; Chaturvedi, M.C. Contribution of constitutional liquation of gamma prime precipitate to weld HAZ cracking of cast Inconel 738 Superalloy. *Scr. Mater.* **2004**, *50*, 641–646, 10.1016/j.scriptamat.2003.11.025.
9. Ojo, O.A.; Chaturvedi, M.C. On the role of liquated γ' precipitates in weld heat affected zone microfissuring of a Nickel-based superalloy. *Mater. Sci. Eng. A* **2005**, *403*, 77–86, 10.1016/j.msea.2005.04.034.
10. Li, Q.G.; Lin, X.; Wang, X.H.; Yang, H.O.; 1, Song, M.H.; Huang, W.D. Research on the grain boundary liquation mechanism in heat affected zones of laser forming repaired K465 Nickel-Based superalloy. *Metals* **2016**, *6*, 64, 10.3390/met6030064.
11. Tancret, F. Thermo-Calc and Dictra simulation of constitutional liquation of gamma prime (γ') during welding of Ni Base superalloys. *Comput. Mater. Sci.* **2007**, *41*, 13–19, 10.1016/j.commatsci.2007.02.008.
12. Li, X.L.; Liu, J.W.; Zhong, M.L. Research on laser cladding superalloy K403. *Appl. Laser* **2002**, *22*, 283–286.
13. Zhou, Z.H.; Zhu, B.D. The study on the laser cladding process and cracking of cast Ni-Based superalloy K3. *J. Mater. Eng.* **1996**, *1*, 32–35.
14. Yang, J.J.; Li, F.Z.; Wang, Z.M.; Zeng, X.Y. Cracking behavior and control of Rene 104 superalloy produced by direct laser fabrication. *J. Mater. Process. Technol.* **2015**, *225*, 229–239, 10.1016/j.jmatprotec.2015.06.002.
15. Zhou, S.F.; Xu, Y.B.; Liao, B.Q.; Sun, Y.J.; Dai, X.Q.; Yang, J.X.; Li, Z.Y. Effect of laser remelting on microstructure and properties of WC reinforced Fe-based amorphous composite coatings by laser cladding. *Opt. Laser Technol.* **2018**, *103*, 8–16, 10.1016/j.optlastec.2018.01.024.
16. Gao, W.Y.; Zhao, S.S.; Wang, Y.B.; Liu, F.L.; Zhou, C.Y.; Lin, X.C. Effect of re-melting on the cladding coating of Fe-based composite powder, *Mater. Des.* **2014**, *64*, 490–496, 10.1016/j.matdes.2014.08.004.
17. Zhang, Y.Y.; Lin, X.; Wang, L.L..; Wei, L.; Liu, F.G.; Huang, W.D. Microstructural analysis of Zr55Cu30Al10Ni5 bulk metallic glasses by laser surface remelting and laser solid forming. *Intermetallics* **2015**, *66*, 22–30, 10.1016/j.intermet.2015.06.007.
18. Wang, Q.Y.; Xi, Y.C.; Zhao, Y.H.; Liu, S.; Bai, S.L.; Liu, Z.D. Effects of laser re-melting and annealing on microstructure, mechanical property and corrosion resistance of Fe-based amorphous/crystalline composite coating, *Mater. Charact.* **2017**, *127*, 239–247, 10.1016/j.matchar.2017.03.011 .
19. Li, R.F.; Jin, Y.J.; Li, Z.G.; Zhu, Y.Y.; Wu, M.F. Effect of the remelting scanning speed on theamorphous forming ability of Ni-based alloy using laser cladding plus a laser remelting process, *Surf. Coat. Technol.* **2014**, *259*, 725–731, 10.1016/j.surfcoat.2014.09.067.

Peer-reviewed version available at *Coatings* **2019**, *9*, 71; doi:10.3390/coatings9020071

20. Choi, J.P.; Shin, G.H.; Yang, S.G.; Yang, D.Y.; Lee, J.S.; Brochu, M.; Yu, J.H. Densification and microstructural investigation of Inconel 718 parts fabricated by a selective laser melting. *Powder Technol.* **2017**, *310*, 60-66, 10.1016/j.powtec.2017.01.030.
21. Li, Q.G.; Lin, X.; Liu, F.C.; Huang, W.D. Microstructural characteristics and mechanical properties of laser solid formed K465 superalloy. *Mater. Sci. Eng. A* **2017**, *700*, 649-655, 10.1016/j.msea.2017.05.064.
22. Montazeri, M.; Ghaini, F.M. The liquation cracking behavior of IN738LC superalloy during low power Nd:YAG pulsed laser welding. *Mater. Charact.* **2012**, *67*, 65-73, 10.1016/j.matchar.2012.02.019.
23. Gong, L.; Chen, B.; Du, Z.H.; Zhang, M.S.; Liu, R.C.; Liu, K. Investigation of solidification and segregation characteristics of cast Ni-Base superalloy K417G. *J. Mater. Sci. Technol.* **2018**, *34*, 541-550, 10.1016/j.jmst.2016.11.009.
24. Gong, L.; Chen, B.; Yang, Y.Q.; Du, Z.H.; Liu, K. Effect of N content on microsegregation, microstructure and mechanical property of cast Ni-base superalloy K417G. *Mater. Sci. Eng. A* **2017**, *701*, 111-119, 10.1016/j.msea.2017.06.044.
25. Basak, A.; and Das, S.; Microstructure of nickel-base superalloy MAR-M247 additively manufactured through scanning laser epitaxy (SLE). *J. Alloys Compd.* **2017**, *705*, 806-816, 10.1016/j.jallcom.2017.02.013.
26. Carter, L.N.; Martin, C.; Withers, P.J.; Attallah, M.M. The influence of the laser scan strategy on grain structure and cracking behavior in SLM powder-bed fabricated nickel superalloy. *J. Alloys Compd.* **2014**, *615*, 338–347, 10.1016/j.jallcom.2014.06.172.
27. Dadbakhsh, S.; Hao, L. Effect of hot isostatic pressing (HIP) on Al composite parts made from laser consolidated Al/Fe2O3 powder mixtures. *J. Mater. Process. Technol.* **2012**, *212*, 2474–2483, 10.1016/j.jmatprotec.2012.06.016.
28. Zhao, X.M.; Chen, J.; Lin, X.; Huang, W.D. Study on microstructure and mechanical properties of laser rapid forming Inconel 718. *Mater. Sci. Eng. A* **2008**, *478*, 119–124.
29. Ola, O.T.; Ojo, O.A.; Chaturvedi, M.C. Role of filler alloy composition on laser arc hybrid weldability of nickel-base IN738 superalloy. *Mater. Sci. Technol.* **2014**, *30*, 1461–1469, 10.1179/1743284713Y.0000000436.
30. Wei, K.W.; Gao, M.; Wang, Z.M.; Zeng, X.Y. Effect of energy input on formability, microstructure and mechanical properties of selective laser melted AZ91D magnesium alloy. *Mater. Sci. Eng. A* **2014**, *611*, 212-222, 10.1016/j.msea.2014.05.092.
31. Alimardani, M.; Fallah, V.; Iravani-Tabrizipour, M.; Khajepour, A. Surface finish in laser solid freeform fabrication of an AISI 303L stainless steel thin wall. *J. Mater. Process. Technol.* **2012**, *212*, 113–119, 10.1016/j.jmatprotec.2011.08.012.
32. Hussein, A.; Hao, L.; Yan, C.; Everson, R. Finite element simulation of the temperature and stress fields in single layers built without-support in selective laser melting. *Mater. Des.* **2013**, *52*, 638–647, 10.1016/j.matdes.2013.05.070.
33. Zhou, Z.P.; Huang, L.; Shang, Y.J.; Li, Y.P.; Jiang, L.; Lei, Q. Causes analysis on cracks in nickel-based single crystal superalloy fabricated by laser powder deposition additive manufacturing. *Mater. Des.* **2018**, 160, 1238-1249, 10.1016/j.matdes.2018.10.042.
34. Ojo, O.A.; Richards, N.L.; Chaturvedi, M.C. Microstructural study of weld fusion zone of TIG welded IN 738LC nickel-based superalloy. *Scr. Mater.* **2004**, *51*, 683-688, 10.1016/j.scriptamat.2004.06.013.
35. Ramirez, A.J.; Lippold, J.C. High temperature behavior of Ni-base weld metal Part II – Insight into the mechanism for ductility dip cracking. *Mater. Sci. Eng. A* **2004**, *380,* 245–258, 10.1016/j.msea.2004.03.075.